SENSORS

Miniature magneto-ultrasonic machines for wireless robotic sensing and manipulation

Xurui Liu[1,2]†, Hanchuan Tang[1]*†, Na Li[1], Linjie He[1], Ye Tian[1], Bo Hao[2], Junnan Xue[2], Chaoyu Yang[2], Joseph Jao Yiu Sung[3], Li Zhang[2,4]*, Jianfeng Zang[1,5]*

Intelligent miniature systems capable of wireless sensing and manipulation hold considerable promise for advancing biomedical applications. However, the development of these systems has been substantially hindered by sensing-actuation incompatibility at small scales. To overcome this challenge, we propose a robotic sensing approach that integrates embedded ultrasonic soft sensors (EUSSs) with magnetic actuators, resulting in a wireless sensor-integrated miniature machine with seamless integration and minimal interference between fields. The EUSS, with its compact dimensions (1.3 millimeters by 1.3 millimeters by 1.6 millimeters), softness (98 kilopascals), and lightweight design (4.6 milligrams), is compatible with both soft and rigid components in terms of deformability and size. By engineering onboard transducers and using passive ultrasound communication along with external magnetic fields, we could wirelessly detect and regulate environmental parameters such as force, vibration, viscosity, and temperature. Demonstrations in rabbit and porcine models show the potential for robotic feedback control, accurate drug dosing, and in situ physiological monitoring, paving the way for real-world applications of intelligent miniature machines.

INTRODUCTION

Miniature machines, typically just a few millimeters in size, have attracted considerable attention because of their high degrees of freedom and compactness, making them ideal for use in confined and hard-to-reach areas (*1*–*3*). These miniature machines are expected to revolutionize medical interventions by overcoming the limitations of traditional tethered methods, such as endoscopy, particularly in terms of accessibility and long-term manipulation (*4*). For example, they could perform direct, real-time monitoring with high spatial resolution, sensing deep-tissue biomechanical and biochemical properties (*5*–*7*), thus providing dynamic feedback to guide therapies and monitor disease progression. Moreover, precise drug delivery systems embedded within these platforms could achieve accurate control over timing and dosage, minimizing off-target effects and maximizing therapeutic efficacy in treatments such as chemotherapy or localized immunotherapy (*8*). Therefore, this capability supports precise treatment delivery, patient safety, and improved therapeutic outcomes.

Magnetic actuation enables compact systems with fast, wireless, and precise control of force and torque, thereby improving the deformability and mobility of miniature robots (*9*–*13*). However, miniature machines are required to integrate effective feedback control, sensory capabilities, and data transmission to function effectively in an in vivo environment. Cointegrating communication and sensing with external magnetic actuation is difficult at small scales. For example, although wireless bioelectronic systems provide real-time data acquisition (*14*–*17*), precise environmental interaction (*18*), and autonomous operation in challenging environments (*19*), most still rely on onboard batteries that add mass and volume and degrade magnetic maneuverability (*15*, *20*). Battery-free approaches, such as electromagnetic coupling, are promising, but transmission interference and short communication ranges (<10 cm) remain limiting (*17*, *21*). In parallel, recent advances in magnetomechanical resonators have opened opportunities for tracking and sensing in miniature devices (*22*). However, their integration into magnetic miniature machines is challenging because of interference from nearby ferromagnetic objects, which can shift resonance frequencies and reduce sensing accuracy. By contrast, ultrasound sensors penetrate deeply and are insensitive to magnetic fields, making them attractive for wireless sensing of physiological signals (*23*–*26*). Nevertheless, the lack of effective robotic transduction and integration schemes has hindered the development of miniature machines for interventional and implantable applications. As a result, achieving advanced functionalities, such as feedback micromanipulation, in situ physiological monitoring and regulation, and targeted dose sensing and delivery, remains a challenge.

In this study, we introduce a robotic sensor approach, as illustrated in Fig. 1 and movie S1, combining embedded ultrasonic soft sensors (EUSSs) and magnetic actuators for a prototype design of miniature machines. This method simultaneously achieves wireless sensing and manipulation of miniature machines without onboard electronics or traditional digital/analog communication at a small scale. EUSSs have a two-dimensional phononic crystal structure (*23*, *27*, *28*) that incorporates air chambers as periodically arranged scatterers embedded within a soft polymer matrix (silicone rubber) (fig. S1). This design facilitates passive communication with ultrasonic waves and enables extreme miniaturization by incorporating microbubble arrays into the magnetic machine (Fig. 1A). Unlike traditional hydrogel-swelling methods used to induce microdeformations in ultrasonic sensors, our approach integrates the actuator component as a direct interface between the sensing unit and the environment. This integration not only broadens the range of

[1]School of Integrated Circuits and Wuhan National Laboratory for Optoelectronics, Huazhong University of Science and Technology, Wuhan, China. [2]Department of Mechanical and Automation Engineering, Chinese University of Hong Kong, Shatin, New Territories, Hong Kong SAR, China. [3]Lee Kong Chian School of Medicine, Nanyang Technological University, Singapore, Singapore. [4]Department of Surgery, Chinese University of Hong Kong, Shatin, Hong Kong, China. [5]State Key Laboratory of Intelligent Manufacturing Equipment and Technology, Huazhong University of Science and Technology, Wuhan, China.
*Corresponding author. Email: hctang1@hust.edu.cn (H.T.); lizhang@cuhk.edu.hk (L.Z.); jfzang@hust.edu.cn (J.Z.)
†These authors contributed equally to this work.

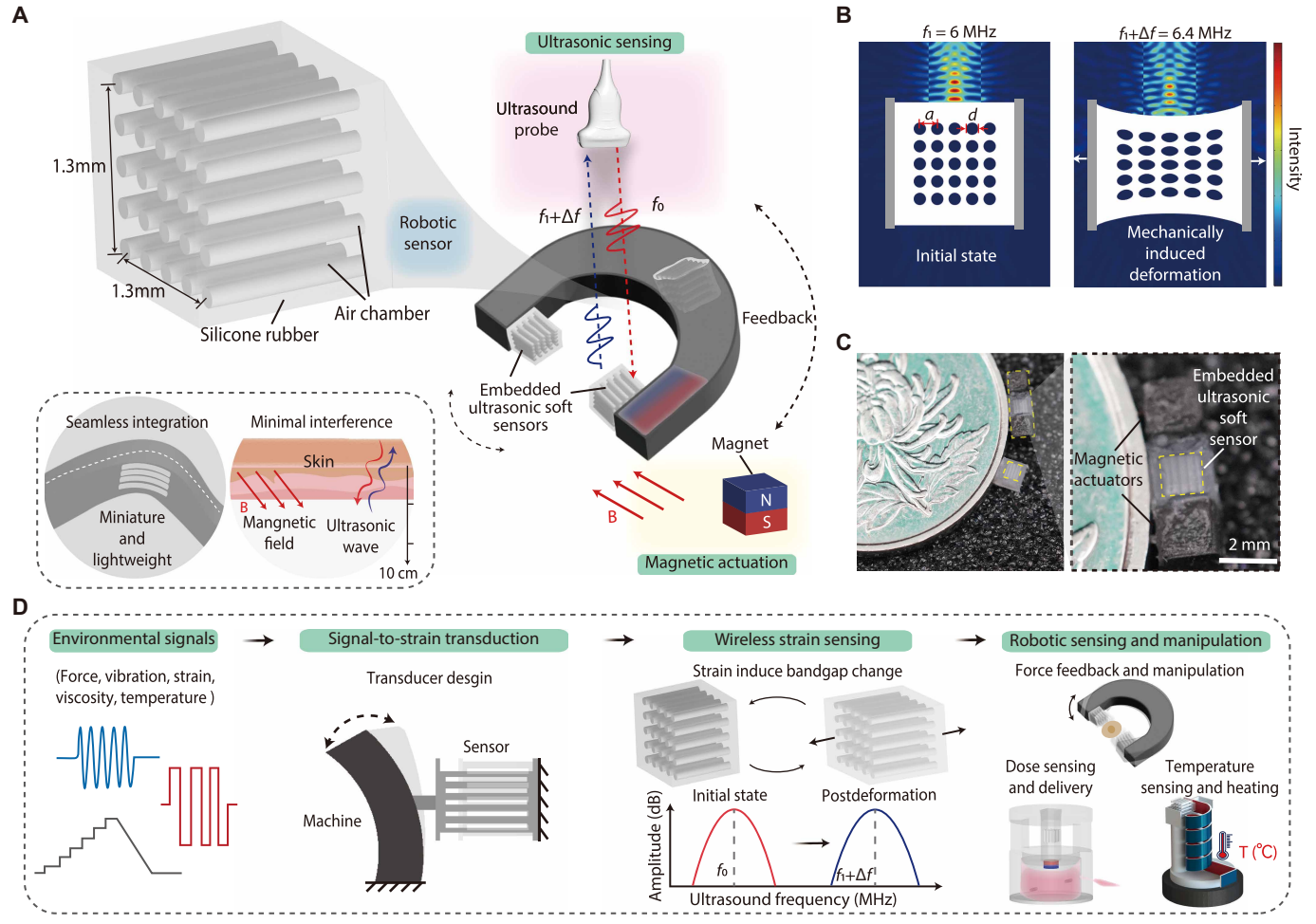

Fig. 1. Mechanism of miniature magneto-ultrasonic machines for wireless robotic sensing and manipulation. (**A**) The concept of EUSSs integrates with a miniature magnetic machine for wireless robotic sensing and manipulation. (**B**) A simulation of the sound scatter field shows the EUSS before and after mechanically induced deformation. (**C**) A photograph illustrates the EUSS and the robotic sensor demonstrator next to a coin with a 30-mm diameter. Scale bar, 2 mm. (**D**) The workflow of our system converts environmental signals—such as mechanical forces, vibrations, strains, and physiological factors like viscosity and temperature—into mechanical strain through a sensor-integrated machine. This strain actively modulates the bandgap of the EUSS, and the corresponding ultrasound response is then captured by an ultrasound probe.

physical parameters that can be detected, such as force, vibration, viscosity, and temperature, but also enhances capabilities for feedback-driven robotic manipulation, accurate dose sensing and delivery, and in situ physiological monitoring and regulation. The EUSS effectively reflects ultrasound waves within a specific frequency range, leveraging the structure-related phononic bandgap (figs. S2 to S6). The final EUSS design is a compact cubic structure measuring 1.3 mm by 1.3 mm by 1.6 mm and weighing 4.6 mg (Fig. 1C and fig. S7). The robotic sensing system, using magnetic actuator-induced microdeformation of the EUSS, converts environmental signals into strain changes, which are detected as frequency shifts in the ultrasound response (Fig. 1D).

RESULTS

Design and workflow of a magnetomotive ultrasound imaging system for robotic sensing

We designed the magnetomotive ultrasound imaging system in three stages (fig. S8). First, a linear array ultrasound probe, mounted on a six–degree-of-freedom (DoF) robotic arm, was used to capture images and track miniature machines. The robotic arm allowed precise maneuvering to select the ultrasound imaging plane accurately. Second, a custom-designed graphical user interface was implemented to fine-tune ultrasound parameters, which optimized the collection of radio frequency (rf) data. The system's core was an ultrasound imaging probe that emitted targeted ultrasound signals at specific frequencies, coupled with specialized software for managing the ultrasound interface and handling the acquisition and analysis of backscattered data. This software provides extensive control over various settings of the ultrasound imaging probe, including window size and position, depth, gain, focus, frequency, line density, and rf scan lines, allowing for customization to meet the specific needs of each imaging scenario. The final stage involves postprocessing the collected raw rf data. A fast Fourier transform (FFT) was applied to analyze multiple rf lines in the time domain. In the frequency domain, specific frequencies were filtered, and the peak frequency was selected as a function of collection time. This comprehensive approach ensured high precision in data acquisition and analysis,

which was critical for effective ultrasound-based sensing in miniature robotics. To evaluate the noise-signal ratio of our system, we measured the echo frequency of the EUSS in a stable environment over several seconds and calculated the SD (σ) of the dataset (fig. S9). The σ value was found to be 124.8 Hz. Using the three-sigma rule to detect outliers, we determined that the detection limit for the echo frequency was 374.4 Hz.

Characterization of EUSSs

To evaluate the ultrasonic communication performance, an EUSS was placed in a water tank to simulate the acoustic impedance of soft tissue (around 1.5 MRayl). We characterized the sensor's response within a spherical coordinate system (Fig. 2A), analyzing the backscattering signal variations with changes in both the tilt angle (θ) and the rotation angle (φ) at different incident angles (fig. S10). At normal incidence, where both θ and φ were zero, the echo peak frequency remained stable at around 6.13 MHz. When θ was fixed at 0° and φ varied from 0° to 45°, the echo peak frequency showed minimal fluctuation (Fig. 2B). However, when θ was set to 15°, changes in φ induced measurable variations in the lattice constants of the phononic crystal, thereby affecting its reflection characteristics. Our experiments confirmed that at an incident angle of less than 15°, the echo peak frequency decreased from 5.93 to 5.72 MHz as φ varied from 0° to 45°. This pronounced angle dependence enabled us to accurately determine the normal incidence angle on the basis of the echo peak frequency fluctuations, ensuring precise system alignment (figs. S11 to S13).

The intensity of the backscattering signal also varied across different rotational angles (Fig. 2C), with maximum amplitude observed only at normal incidence. Symmetrical incident angles (θ and −θ) exhibited similar peaks and valleys within the frequency spectrum, particularly between 5 and 7 MHz (Fig. 2D), demonstrating structural symmetry. When scanning at these angles and recording the frequencies, consistent spectral features were noted. Ultrasound parameters were further adjusted to five scanning lines with 0.4-mm spacing, and the root mean square error (RMSE) of the base frequency (f_0) was analyzed (fig. S14). At a tilt angle of 0° (normal incidence), RMSE was minimized to 0.032 MHz. The σ values for angles from 0° to 15° were consistent with those from 0° to −15°, reflecting the sensor's structural symmetry.

This characterization protocol enabled optimization of the ultrasound beam incident on the EUSS on the basis of the echo peak frequency. Because our sensing approach relied on ultrasound imaging, all measurements were enhanced by real-time ultrasound feedback. After identifying the area of interest from the ultrasound image, ultrasound scanning parameters were set to acquire rf data. For larger tilt angle adjustments, an external mechanical arm or displacement platform was used. The finer adjustments were made electronically by controlling the ultrasound incident angles. The base frequency (f_0) of the echo peak shifted accordingly, with the lowest frequency established as the baseline for subsequent tests.

We evaluated the surrounding interference and frequency selectivity of the EUSS against various materials with moduli ranging from kilopascals to gigapascals, mimicking the spectrum from soft tissue to bone in the human body. Despite its low modulus (98 kPa), the EUSS produced a strong reflected signal compared with a rigid magnet with a much higher Young's modulus in the gigapascal range (Fig. 2E). To improve the localization and sensing capabilities of the sensor, we integrated ultrasound imaging with frequency mapping (Fig. 2, F and G), enabling differentiation from other reflected intensity signals by measuring the central reflected frequency near 6 MHz. Unlike the magnet, which reflected a broad bandwidth because of its lack of frequency-selective echo reflection, the EUSS uniquely reflected echoes around 6 MHz. This high acoustic impedance and selective reflection made the EUSS an effective tool for ultrasonic sensing under biologically relevant conditions. We further assessed the ultrasonic communication distance of the EUSS by submerging it more than 10 cm deep in a water tank and testing it through fresh ex vivo porcine tissue (fig. S15). The backscattering signal was captured and analyzed using FFT, which revealed robust backscattering within a narrow, selective frequency range.

Systematic cyclic loading analysis was performed on the EUSS to evaluate its strain-frequency hysteresis characteristics. Under controlled triaxial loading protocols, the system was subjected to progressively increasing strains of 2, 5, 10, 15, and 20% with triplicate measurements at each threshold (Fig. 2, H and I). We also examined the selection of scan lines during strain testing, and all scan lines showed corresponding peak frequency shifts under strain (fig. S16). For resolution characterization, superimposed perturbation experiments were implemented with a 5% preload baseline. Notably, subpercentile strain increments of 0.1 and 0.2% induced average frequency deviations of 4970.6 and 11,032.7 Hz, respectively (Fig. 2J).

In our robotic sensor design, we adopted a quasistatic sensing mode in which the actuation component induced controlled, confined deformation of the EUSS, with constraints applied to enable single-axis deformation. The sensing module was activated only after the system had reached a stable state, ensuring that signal acquisition was unaffected by motion (such as tilting, rotation, and displacement). This approach enabled precise capture of target environmental signals and effectively minimized noise from dynamic processes. Our assembly strategy of the EUSS and the magnetic actuator was systematically guided by the targeted application scenarios of the robotic platform (fig. S17 and Supplementary Methods).

Miniature grippers for wireless force sensing and feedback pick-and-place manipulation

Clinical grippers were commonly used for tissue sampling and manipulation (*29*). However, improper grasping forces could lead to a high rate of complications (*30*). Through magnetic actuation, these grippers could be controlled wirelessly, enhancing their functionality and range of application (*31*). Although magnetic actuation allowed these grippers to be controlled wirelessly, integrating wireless force sensing remained challenging because of issues with sensitivity, size, and actuation-sensing compatibility.

We present a miniature gripper integrated with two EUSSs for wireless actuation and force sensing (Fig. 3A). The gripper's actuating mechanism is made from a ferromagnetic soft polymer with specific magnetization patterns (fig. S18). Upon contacting a sample, the EUSS deformed because of the elasticity of the material. Unlike rigid sensors, the soft EUSS material provides gentle, conformal contact with delicate objects, such as salmon eggs (3 mm in diameter), minimizing the risk of damage. The deformation of the EUSS was measured by our ultrasonic sensing system to calculate the force acting on the gripper. Force calibration using a commercial force sensor demonstrated a force sensitivity of 6100 Hz/mN and a force resolution of 61.3 μN (fig. S19 and Supplementary Methods).

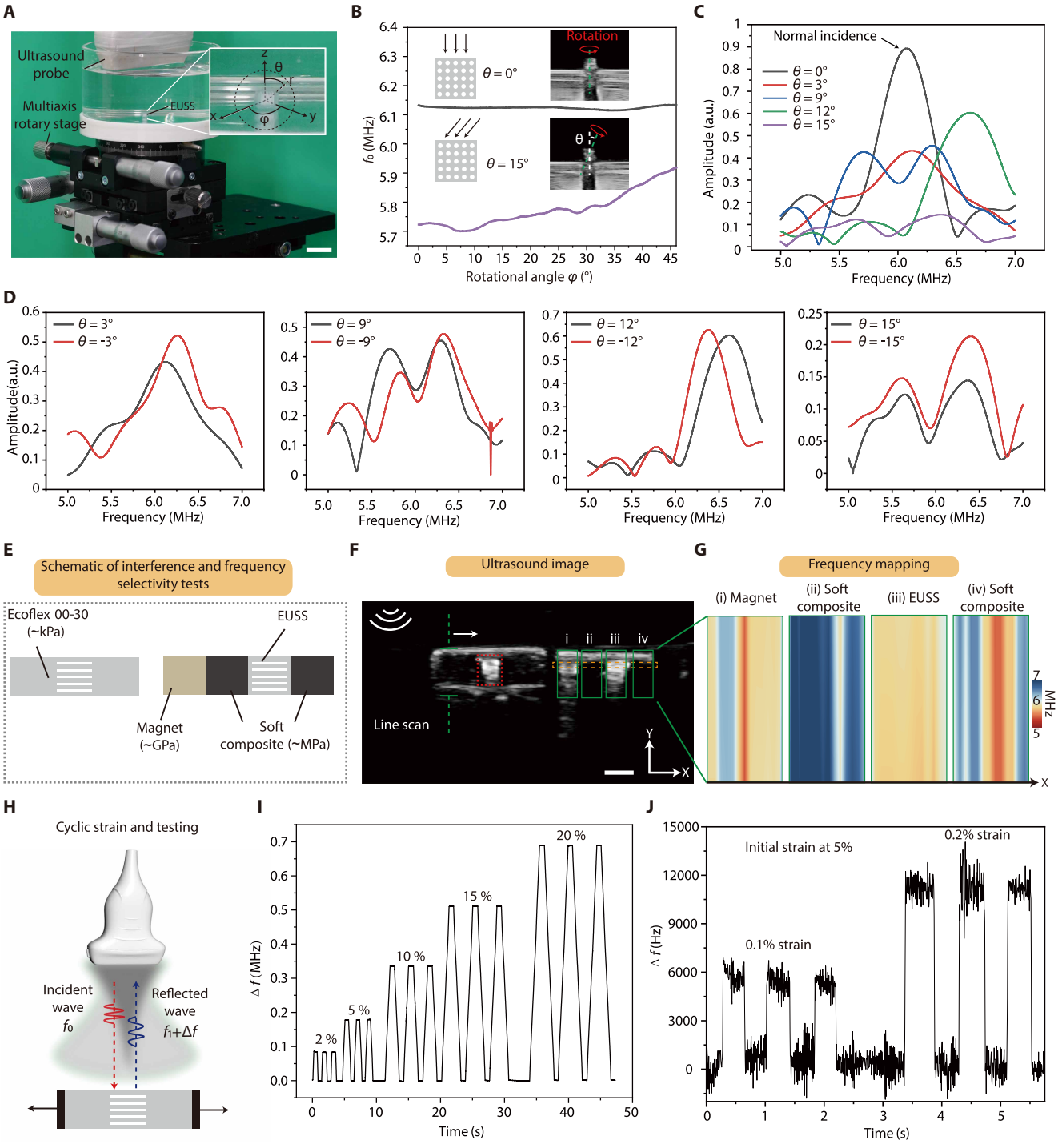

Fig. 2. Characterization of EUSS. (**A**) The experiment setup for misalignment testing. The sensor (EUSS) was centrally positioned in a water tank, which was mounted on a multiaxis rotary stage with three DoFs. This setup allowed for precise horizontal and vertical translation, as well as rotation around the vertical axis. The ultrasound probe was placed above the water tank. Scale bar, 10 mm. (**B**) Base frequency (f_0) was obtained by scanning the rotational angle within a quarter cycle. By varying φ from 0° to 45° and keeping θ fixed at 0°, the echo peak frequency remained nearly constant at ~6.13 MHz. When θ was set to 15°, the echo peak frequency exhibited a gradual increase from 5.75 MHz to around 6.0 MHz as φ varied from 0° to 45°. (**C**) The intensity of the backscattering signal varied across different incident angles. Only the signals backscattered from waves at a normal incidence (θ = 0°) exhibited maximum amplitude. Amplitudes are reported in arbitrary units (a.u.). (**D**) Symmetric incident angles (θ and −θ) display similar peaks and valleys within the frequency spectrum, particularly between 5 and 7 MHz. (**E**) Comparison of the ultrasound tracking capabilities between EUSS and other different modulus materials (ranging from kilopascals to gigapascals). (**F**) Ultrasound imaging of EUSS and other materials with different moduli. Scale bar, 2 mm. (**G**) Frequency mapping of ultrasound images (green box). (**H**) Schematic representation of cyclic strain testing of EUSS. (**I**) Experimental data showing the frequency shift of EUSS under various strains: 2, 5, 10, 15, and 20%. (**J**) Experimental data of EUSS subjected to a constant base strain of 5% with additional minor strains of 0.1 and 0.2% applied.

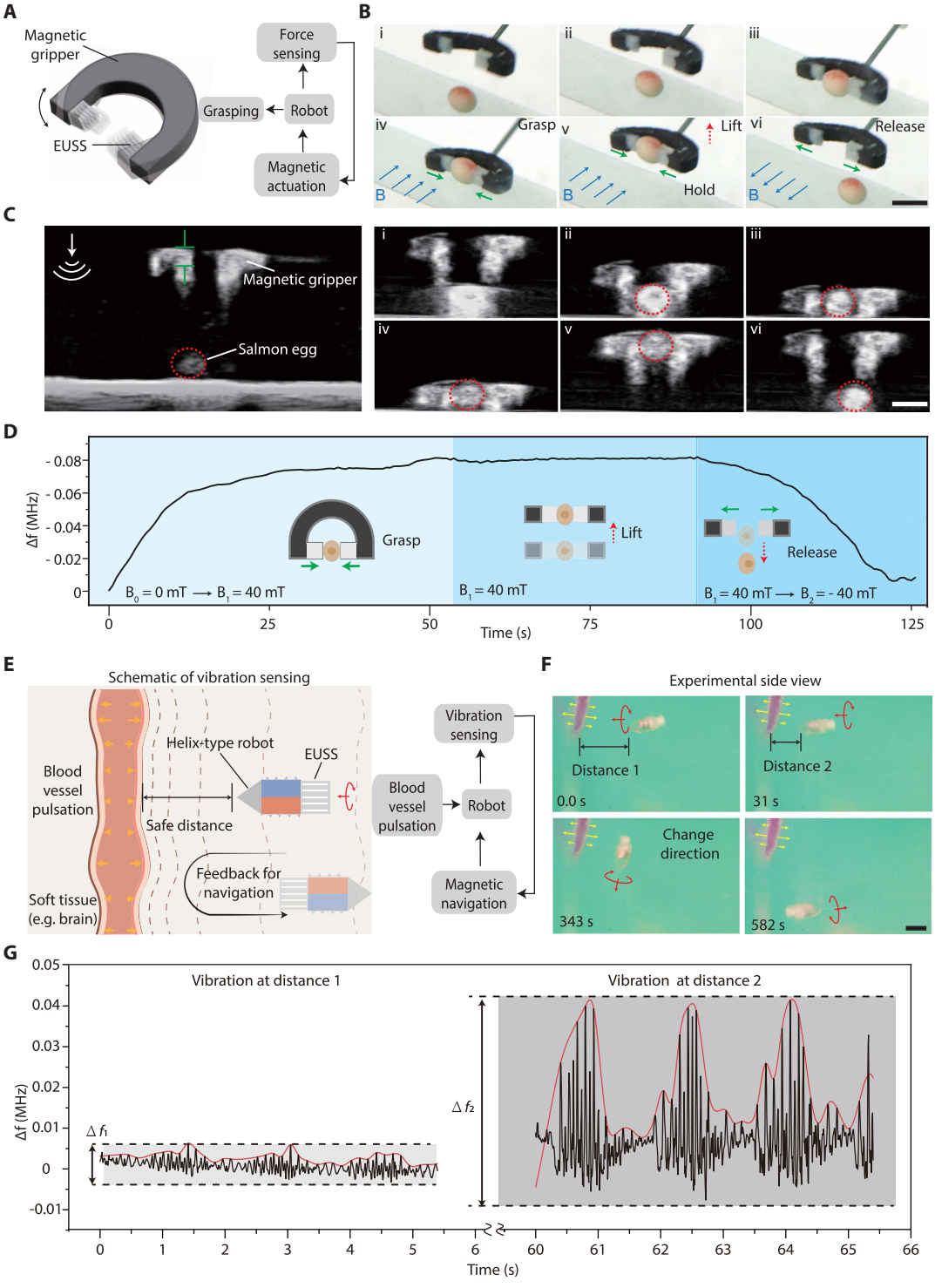

Fig. 3. Miniature machines for wireless force and vibration sensing. (**A**) Schematic of a magnetic soft gripper for pick-and-place operations with force feedback. (**B**) Photographs illustrate a magnetic soft gripper picking and placing a salmon egg with wireless force sensing. Scale bar, 5 mm. (**C**) Ultrasound imaging of the magnetic soft gripper grasping, lifting, and releasing a salmon egg. Scale bar, 5 mm. (**D**) The echo frequency was recorded during the pick-and-place operation with a magnetic soft gripper handling a salmon egg. (**E**) Schematic top view of magnetic helix-type robot feedback navigation in soft brain tissue. The amplitude of blood vessel pulsation indicates the distance between the robot and the vessel. Vibration detection from the robotic sensor helps monitor safe distances. (**F**) Experimental side view of magnetic helix-type robot feedback navigation in a soft tissue phantom. Scale bar, 5 mm. (**G**) Blood vessel pulsation system vibration monitored by a magnetic helix-type robot with an EUSS at various distances. The echo frequency shift (Δf_1) is around 0.005 MHz, which is substantially smaller than the frequency shift (Δf_2) (more than 0.04 MHz).

To demonstrate feedback-based wireless force control, we conducted pick-and-place manipulation of salmon eggs, guided by ultrasound imaging and sensing (Fig. 3B and movie S2). The gripper was accurately navigated to the target location, where it successfully executed grasping, holding, and releasing operations while continuously monitoring the contact force via the ultrasound system (Fig. 3, C and D). All manipulations were performed under in-plane ultrasound imaging guidance (fig. S20). We simultaneously scanned five rf lines to eliminate interference and misalignment, consistently finding that the middle line provided the optimal signal. The force feedback ensured that the exerted force on the salmon eggs remained below the cellular rupture threshold (fig. S21). Our design introduced a wireless force-sensing method for miniature systems that not only provided force feedback during operations but also offered a potential solution for in situ measurement of tissue mechanics (*5*).

Miniature helix-type robots for wireless vibration sensing and feedback navigation

Many physiological signals, such as heartbeats and vascular pulses, were inherently dynamic. Leveraging the high temporal resolution of EUSS, we could effectively measure these vibration signals. To emphasize the importance of vibration sensing, we proposed a feedback navigation method for wireless magnetic robots in a brain model (*32*, *33*). To enable effective penetration of soft tissue, these robots were designed with a helical casing and a conical tip, enclosing a cylindrical permanent magnet (2 mm in diameter and length). However, without vibration feedback, the conical tip could cause vessel damage during navigation. To mitigate this risk, we developed a compact design that incorporated vibration sensing capabilities, ensuring precise navigation without compromising actuation performance (Fig. 3E and fig. S22).

To simulate vascular pulsations, an artificial blood vessel (2 mm in diameter) was connected to a pulsatile pump and embedded in a soft tissue phantom. We observed that the signal frequency varied with the robot's distance from the artificial vessel (Fig. 3, F and G; fig. S23; and movie S3). At a remote position (distance 1), the peak frequency variation was minimal ($\Delta f_1 < 0.005$ MHz), indicating a weaker pulse wave. When the robot was closer to the artificial vessel (distance 2), the peak frequency variation increased ($\Delta f_2 > 0.04$ MHz). This frequency shift provided a navigational cue for the feedback control of the robots, with the measured signals being dependent on the flow rate (fig. S24).

Miniature capsule robots for wireless dose sensing and target delivery in vivo

Effective drug delivery is essential for modern medical treatments, aiming to maximize therapeutic efficacy and minimize side effects (*34*–*39*). Developing mechanoresponsive systems that can wirelessly deliver drugs with precise control over timing and dosage offers great promise but remains challenging (table S3 and Supplementary Methods). To address these challenges, we developed a robotic sensing method capable of actively releasing and quantifying liquid payloads. The capsule robot featured a storage chamber that held up to 150 μl of liquid, with two 50-μm-diameter apertures on its outer shell for controlled discharge (Fig. 4A and fig. S25). A magnet-embedded piston, connected to a soft strip within the EUSS, enabled both actuation and sensing. Exposure to an external magnetic field moved the piston, reducing the chamber volume and simultaneously stretching the EUSS. Because the liquid is nearly incompressible, the piston's displacement was almost entirely translated into expelled volume. Bringing the magnet closer to the robot enhanced the magnetic field, allowing for multiple controlled releases. Changes in echo frequency were analyzed to accurately measure the volume changes induced by magnetic actuation (Fig. 4B).

We used magnetic control to capsule robots with rolling locomotion in an ex vivo porcine stomach model (movie S4). The robots were navigated to specific sites for the targeted release of their liquid payloads (Fig. 4C and fig. S26). Subsequently, we confirmed the effectiveness of the liquid sample release and precisely monitored its volume. The magnetic field strength was incrementally increased to facilitate sample injections (Fig. 4D, movie S5, Supplementary Methods, and figs. S27 and S28). The echo frequency changes from the EUSS were continuously recorded, displaying a steplike signal pattern. The volumes of the liquid released during each step (V_1 to V_5) were calculated as 2.98, 1.86, 0.735, 0.655, and 0.618 μl, respectively.

To further validate the functionality of the EUSS, we conducted an in vivo targeted delivery experiment in a rabbit's stomach (Fig. 4E and movie S6). The capsule robots were loaded with iodized glycerol to enhance their visibility under fluoroscopic imaging (Fig. 4F). Additionally, we navigated the capsule robots and monitored their echo frequency changes (Δf) during liquid sample release under real-time ultrasound imaging guidance (Fig. 4G). In the initial dosage control release, we performed three dosing trials under external magnetic control, each releasing a dose nearly identical in volume, measured at 4.49, 4.91, and 4.53 μl, respectively (Fig. 4H). After this, our subsequent experiments focused on administering and monitoring a substantially different drug dosage, involving distinct volume changes up to 16.75 μl (fig. S29). These results indicated that our EUSS was both feasible and effective for in vivo drug delivery, offering precise control over timing and dosage.

Miniature viscometer bots for wireless viscosity sensing and manipulation in vivo

The human body contains essential fluids, such as blood and digestive juices, whose viscosity is critical for maintaining health and managing diseases (*40*–*42*). Current methods for monitoring fluid viscosity, like endoscopy, were invasive and not suited for long-term, localized, in situ measurements (*43*). To address this, we developed a viscometer bot capable of wireless in situ viscosity measurement (Supplementary Methods). The robot comprised three main components: a vibrating plate connected to an EUSS, a supporting plate, and a bottom plate (Fig. 5A). The vibrating plate, made from a ferromagnetic soft polymer with predesigned magnetization, connected to the EUSS via a connecting plate. The sensing mechanism relied on the damping effect exerted on a vibrating element in a fluid environment (*44*), where the vibration resistance directly correlated with fluid viscosity (Fig. 5B).

Under an external rotating magnetic field (fig. S30), the oscillating movement of the vibrating plate was converted into the periodic stretch movement of the EUSS (Fig. 5C and movie S7). Because the viscosity of fluid affected the damping of the vibrating element, this viscosity could be calculated on the basis of the frequency change (Δf) of the EUSS (Fig. 5D and fig. S31). The frequency shift (Δf_1-Δf_2) was measured across a range of viscosities, specifically at 1.00, 2.68, 4.10, 5.70, and 7.94 mPa·s. These measurements corresponded to frequency changes of 0.16, 0.14, 0.096, 0.53, and 0.047 MHz, respectively.

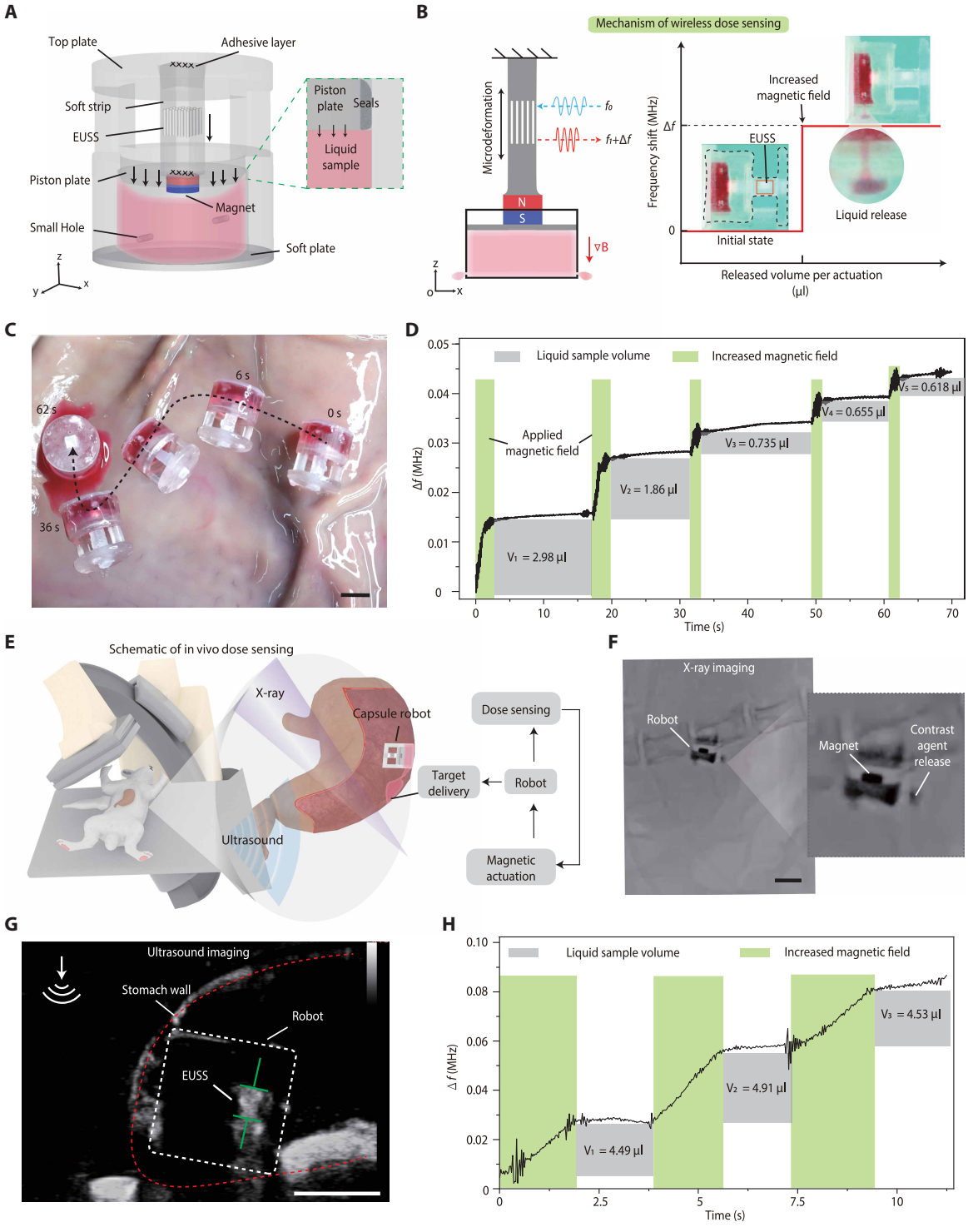

Fig. 4. Miniature capsule robots for wireless dose sensing and target delivery in vitro and in vivo. (**A**) Structural diagram of the capsule robots. Each robot features a storage chamber, a magnet-embedded piston, and a soft strip with an EUSS. (**B**) The mechanism for wireless dose sensing. The release of liquid generates a microdeformation in the EUSS. By detecting the echo frequency shift (Δf), the volume of liquid released per actuation can be calculated. (**C**) Controllable movement and release of the capsule robot for active delivery in an ex vivo porcine stomach. Scale bar, 5 mm. (**D**) Dose sensing in capsule robots with varying volumes of liquid released. (**E**) Schematic overview of in vivo dose sensing. The capsule robot is deployed into a rabbit's stomach, under the guidance of ultrasound and fluoroscopy imaging. (**F**) Radiology images of capsule robots release the liquid sample by an external magnetic field. Scale bar, 5 mm. (**G**) The ultrasound imaging of the capsule robot in the rabbit's stomach. (**H**) Echo frequency shift was recorded for dose sensing of the capsule robot in a rabbit's stomach in vivo.

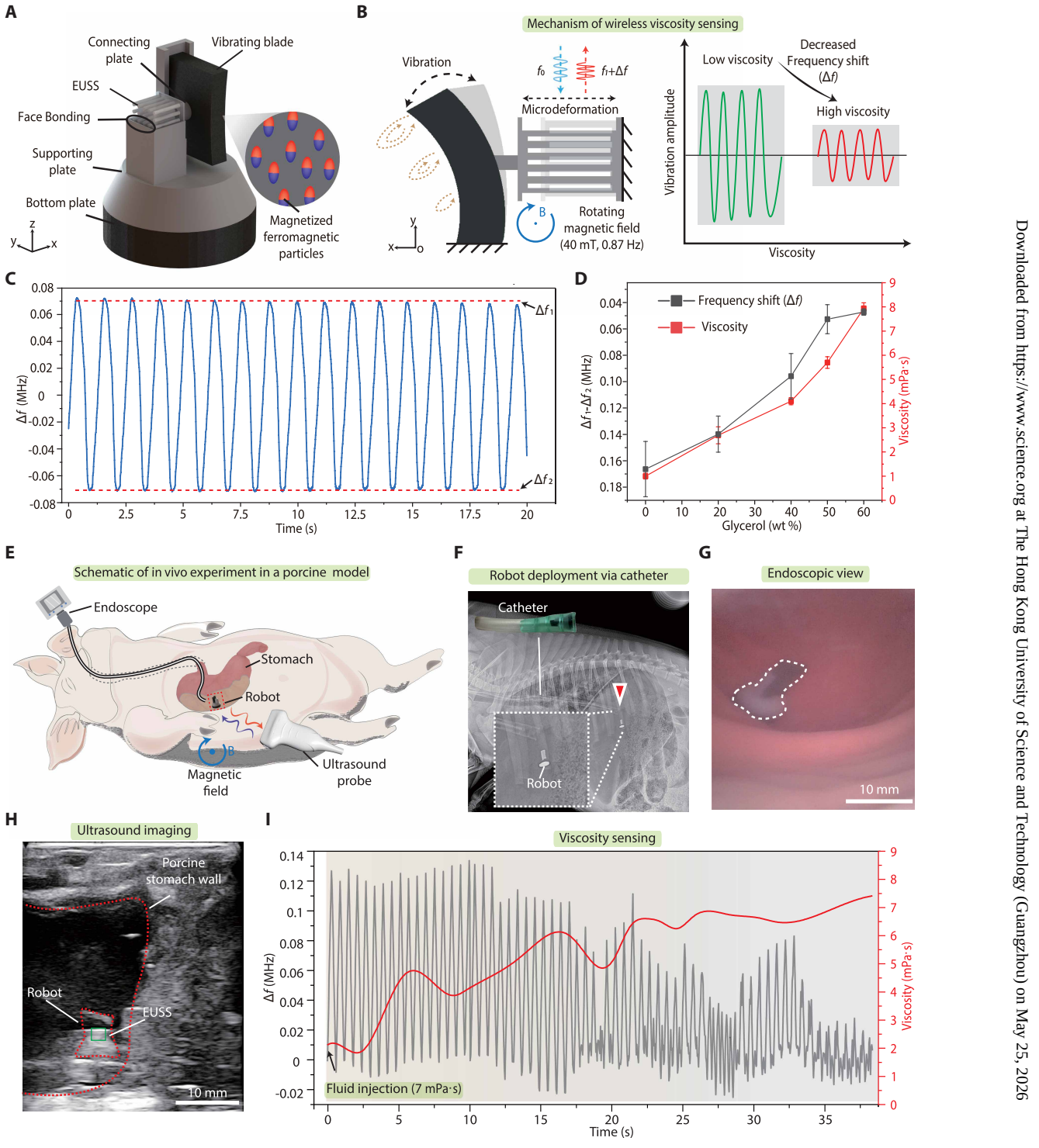

Fig. 5. Miniature viscometer bots for wireless viscosity sensing and manipulation in vitro and in vivo. (**A**) Design of a viscometer bot for wireless detection of environmental viscosity. The robot consists of three main parts: a bottom plate, a vibrating plate with an EUSS, and a supporting plate. (**B**) The mechanism for wireless viscosity sensing. The vibrating plate is connected to the EUSS. A rotating magnetic field induces microdeformation in the EUSS, resulting in a frequency change in the ultrasound signal. Higher fluid viscosity dampens the vibration amplitude because of the increased viscosity force. (**C**) Experimental measurement of periodic frequency signals in a fluid with stable viscosity. (**D**) The relationship between frequency change (Δf_1-Δf_2) and various viscosities from 1 mPa·s to 8 mPa·s. Data are represented as mean values ± SD ($n = 3$ independent samples) (**E**) Schematic of the in vivo experiment in a porcine model. (**F**) Radiology image of the robot validating its deployment into the stomach via a catheter. (**G**) Endoscopic view of the robot in vivo after catheter deployment. Scale bar, 10 mm. (**H**) Ultrasound imaging of the robot in the stomach of a porcine model. The green rectangle indicates the location of the EUSS. (**I**) The frequency shifts (Δf) were recorded throughout the in vivo experiment. The decreased frequency change (Δf_1-Δf_2) signifies higher fluid viscosity.

To further validate the viscosity sensing capability of the robot, we tested its operation in an ex vivo porcine stomach (figs. S32 and S33 and movie S8). By introducing fresh porcine blood (viscosity of around 4 mPa·s) into the environment (viscosity of 5.7 mPa·s) around the robot, we showcased its ability to detect viscosity changes within seconds. We further demonstrated the in vivo application of a viscometer bot within the porcine stomach to measure changes in fluid viscosity (Fig. 5E and figs. S34 and S35; see Materials and Methods for details). The robot was deployed via a catheter under the guidance of fluoroscopy imaging (Fig. 5F, fig. S36, and movie S9). Initially, we calibrated the viscometer bot by injecting a phosphate-buffered saline (PBS) solution through the endoscope. Subsequently, we introduced simulated digestive juices of varying viscosities through the endoscope (Fig. 5G and fig. S37). The simulated digestive juices were chosen with a viscosity of 7 mPa·s to simulate the changes in viscosity associated with ulcers (*45*). The ultrasound system successfully recorded signals indicating changes in viscosity during the in vivo experiments (Fig. 5, H and I).

Magnetic thermometer bots for wireless temperature sensing and heating in vivo

Wireless temperature sensing and regulation have promising applications in biomedicine (*46*, *47*), including in inflammation detection (*48*, *49*) and targeted thermal treatments like tumor ablation and gastric antral vascular ectasia (*50*, *51*). However, the lack of real-time temperature sensing during thermal ablation could lead to serious complications, such as tissue perforation (*52*, *53*). Integrating temperature sensing into wireless miniature machines posed challenges, including limited communication range, large size, and potential sensing interference (table S4 and Supplementary Methods).

Here, we present a robotic sensing method that enabled wireless temperature sensing and remote heating simultaneously (Fig. 6A). The thermometer bot consisted of three main components: an EUSS, a temperature-responsive element, and an actuation segment. The core of the temperature-sensing mechanism was the conversion of thermal variations into mechanical strain on the EUSS, achieved through a helical bimetallic strip made from two metals with distinct thermal expansion coefficients (each averaging 100 μm thick). Changes in ambient temperature caused anisotropic expansion in the strip, leading to a measurable deflection (fig. S38). The helical structure amplified this motion, inducing stretching deformation of the EUSS (Fig. 6B). Consequently, temperature changes in the thermometer bot were quantified by shifts in the ultrasound echo frequency (Fig. 6C). We evaluated the robot's durability and thermal sensitivity, confirming its suitability for real-time temperature monitoring in the range of 30° to 60°C (fig. S39). The bimetallic strips also served dual roles: They amplified the signal and acted as a heat source for hyperthermia applications (Fig. 6D and figs. S40 to S42). At 55°C, the average frequency change was 0.451 MHz, with a temperature sensitivity of 1200 Hz/°C (0.26%/°C) and a resolution of 0.31°C, sufficient for thermal ablation feedback. We further tested the thermometer bot for wireless temperature sensing during thermal ablation on ex vivo porcine liver tissue (Fig. 6, E and F, and fig. S43). Throughout ablation, the robot continuously monitored temperature (Fig. 6G and movie S10), with the results confirming effective localized tissue ablation. To demonstrate the robot's practical utility, we conducted temperature sensing and regulation experiments in a porcine model (Fig. 6, H and I). An rf signal was applied three times, each for 10 s, to simulate in situ temperature regulation. The ultrasound sensing system successfully monitored temperature changes from 36° to 38°C (Fig. 6J).

DISCUSSION

Sensor-integrating machine systems encounter challenges in terms of miniaturization, spatiotemporal resolution, communication range, and sensing-actuation compatibility. This study introduces EUSS integrated with magnetic miniature machines to facilitate the wireless robotic sensing of a wide range of signals, including force, vibration, viscosity, and temperature. Through a series of in vitro and in vivo demonstrations, we confirmed the versatility and applicability of our methods, showcasing their effectiveness in micromanipulation, targeted delivery, and physiological signal monitoring.

The compatibility and stability between the sensor and the miniature machine are crucial. We demonstrated that the EUSS has mechanical robustness and functional stability (fig. S7), making it suitable for integration with miniature machines. Its small size, high strain resolution sensing, and deep communication range, combined with its multifunctionality as a sensor, processor, and antenna, enable efficient wireless embedded sensing in a compact design. This approach enables us to fully integrate the sensor within the actuator without compromising the actuator's performance. We demonstrated various potential applications where sensors are integrated with actuators, each posing unique challenges that current methods struggle to address in micromanipulation, targeted delivery, and physiological signal monitoring. Additionally, the sensitivity and measurement range of the proposed miniature machines can be adjusted through specific design choices. For example, altering the vibrational blade can control the dose-sensing range and sensitivity of viscometer bots. Similarly, varying the size of helical bimetallic elements can affect the temperature-sensing range and sensitivity of thermometer bots. Moreover, the overall design of miniature machines can be optimized to achieve a smaller volume by reducing the size of sensor units or transducers (fig. S44). Overall, our study presents a platform technology for wireless sensor-integrating machine systems. This approach could integrate both proprioception and exteroception into miniature machines, broadening their potential for biomedical applications and paving the way for the development of intelligent miniature machines.

MATERIALS AND METHODS

Objective and study design

The objective of this study was to develop and evaluate a wireless robotic sensing platform based on miniature magneto-ultrasonic machines for biomedical applications. We conducted a series of controlled experiments in which the devices were subjected to various mechanical strains and dynamic conditions. The key parameters were measured and regulated using ultrasound imaging and magnetic actuation. Sample sizes for each experiment were determined through preliminary analyses, and end-point selection was based on the stabilization of the measured parameters over time. Further details on these study components are provided in the following sections.

The fabrication of EUSS

The fabrication of EUSS used a mold casting technique, as illustrated in fig. S1. The process began with the use of a three-dimensional

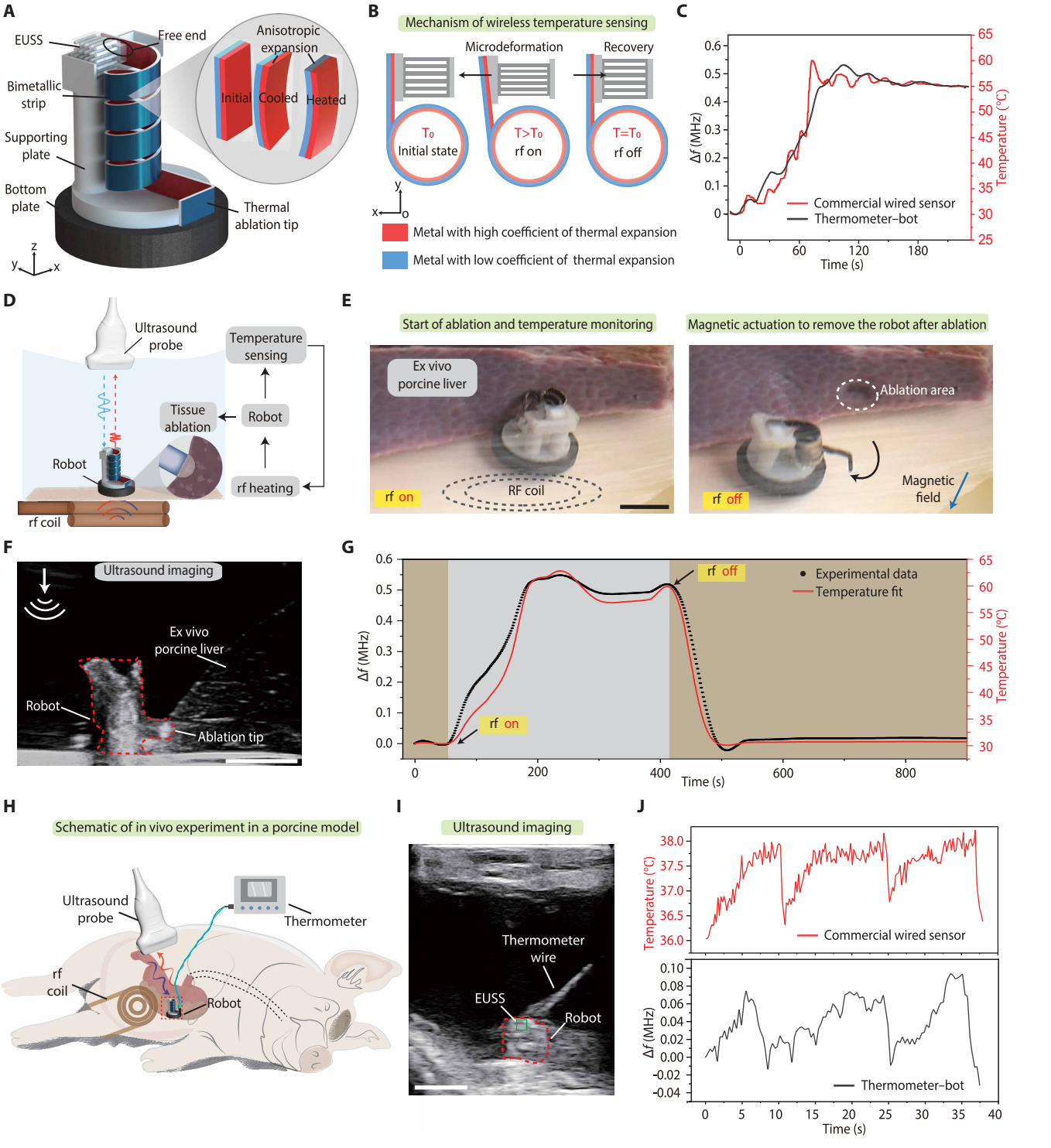

Fig. 6. Magnetic thermometer bots for wireless temperature sensing and thermal ablation in vitro and in vivo. (**A**) Design of a thermometer bot using the proposed EUSS to monitor ablation temperature. The robot comprises three main components: a bottom plate, helical bimetallic strips with an EUSS, and a supporting plate. (**B**) The mechanism for wireless temperature sensing. The deflection of the helical bimetallic strip is correlated with temperature changes in the environment, causing microdeformation in the EUSS. (**C**) The measured frequency change (Δf) of the robot to a change in temperature from 30° to 60°C. (**D**) Schematic of temperature monitoring during thermal ablation for ex vivo thermal ablation. (**E**) The robot was navigated to the target site, where the ablation tip contacted the porcine liver. After 8 min of ablation, the tissue exhibited areas of necrosis. Scale bar, 5 mm. (**F**) The ultrasound imaging of the thermometer bot for ex vivo porcine liver ablation. Scale bar, 10 mm. (**G**) The measured frequency change (Δf) of the robot during thermal ablation of the bimetallic strip. (**H**) The schematic of the in vivo experiment in the porcine model. (**I**) The ultrasound imaging of a robot in the stomach of a porcine model. The green rectangle is the location of the EUSS. Scale bar, 10 mm. (**J**) The wireless temperature regulation by thermal ablation and sensing by an ultrasound system throughout the in vivo experiments.

(3D) printer to create a positive model of the sensor. Ecoflex 00-30 was selected as the casting material because of its exceptional softness and flexibility. This material was then carefully poured into the mold, and the upper part of the sensor was allowed to cure at room temperature for 4 hours. After curing, the component was precisely removed from the mold. To embed an array of air chambers within the soft matrix and effectively seal the sensor's open side, a film with a thickness of 200 μm was spin-coated onto a glass substrate. This film acted as a sealant when the sensor's open side was pressed against it, ensuring an airtight closure. The sealed unit was then cured in an oven at 80°C for more than an hour to achieve a durable bond and finalize the sensor assembly.

The fabrication of magnetic gripper robots

The magnetic actuator was crafted by homogeneously mixing ferromagnetic neodymium-iron-boron (NdFeB) particles with a polydimethylsiloxane (PDMS) polymer matrix (Sylgard 184, Dow Corning) at a 1:1 weight ratio. This magnetic composite was thoroughly stirred for 5 min and then carefully poured into a 3D-printed mold. It underwent a 24-hour curing process on a hot plate set at 60°C. After curing, the magnetic actuator component of the gripper was gently removed from the mold. The actuators were then exposed to a 2.5-T impulse magnetic field using a digital pulse magnetizer, provided by Beijing Eusci Technology Ltd., to achieve magnetization. In the final assembly stage, the EUSS was attached to the magnetic gripper with the aid of adhesive and precise mold assistance, ensuring proper alignment and integration.

The force calibration of magnetic gripper robots

A commercial force sensor was used to calibrate the magnetic gripper robots. The force exerted by the gripper was transmitted to the commercial sensor through a rigid rod. Initially, the sensor was securely positioned against one side of the rod. Activation of a magnetic field prompted the gripper to exert force, causing the sensor to deform. This deformation, and the corresponding force applied, was recorded by the commercial sensor. Throughout the calibration process, an ultrasound probe monitored the peak frequency of the echo. Our experimental findings indicated that our wireless force-sensing technique produced a more refined curve compared with that of the commercial sensor (with a force resolution of 1 mN and a temporal resolution of 50 ms). This suggested that our method offered superior precision in both forces (with a resolution as fine as 0.2 mN and a temporal resolution of 10 ms).

Fabrication and control strategy of the helix-type robot

We engineered a helix-type robot specifically designed for navigation within soft tissue phantoms, propelled by external magnetic forces. This robot featured a cylindrical NdFeB (N52 grade) magnet encased in a 3D-printed shell with a helical structure and a pointed conical tip, and it was equipped with a sensor. The magnet, characterized by radial magnetization, fit precisely into the shell, facilitated by a customized mold. The shell, measuring 2 mm in both diameter and height, ensured a snug fit for the magnet. After the magnet and shell were assembled, the sensor was securely affixed to the shell's exterior using a strong adhesive, completing the robot's assembly.

For this study, we used a six-DoF robotic arm equipped with a magnet and a stepper motor to generate a rotational magnetic field. Upon introducing the robot into the soft tissue phantom, the rotating magnet exerted magnetic force and torque, effectively guiding the robot toward the target. Adjustments to the orientation of the magnet enabled the robots to execute turns, aligning with the changing magnetic fields. An ultrasound probe was used for imaging and sensing the robots throughout their navigation.

Fabrication of soft tissue phantom with biomimetic blood flow

To replicate the mechanical properties of soft tissues, such as the brain, we developed a gelatin-based model. This involved blending 5.1 wt % gelatin powder from Sinopharm Chemical Reagent Co. Ltd. with hot water at 90°C for 10 min. After thorough mixing, we poured the solution into an acrylic container to set. To simulate an artificial artery system, we used a silicone rubber tube with an inner diameter of 2 mm, a wall thickness of 0.25 mm, and a Young's modulus of 1 MPa. This tube was connected to a peristaltic pump and was arranged in the setting gelatin before it cooled to room temperature (23°C), solidifying into a gelatinous state. We achieved biomimetic blood flow by circulating simulated blood at a rate mimicking 100 beats per minute, closely emulating the conditions found within human tissues.

Fabrication and manipulation of the capsule robot

The capsule robot was composed of a body, piston, and bottom cap, all manufactured from 3D-printed resin. It featured a soft strip made from Ecoflex with an EUSS. A small aperture at the bottom of the capsule facilitated the release of liquids. Operating the robot involved two primary functions: navigating the terrain and managing liquid discharge. The robot used a tumbling motion for movement, a method previously identified in the literature as effective for traversing complex physiological terrains. When a magnetic field (**B**) was applied, the robot's cylindrical surface interacted with its surroundings (fig. S25), causing it to roll as the net magnetic moment (**M**) aligned with the magnetic field. We demonstrated this capability by directing the robot to maneuver over ex vivo porcine tissue that was characterized by its varied dry, wet, and rugged conditions. The robot was guided along a curved path to a predetermined site. Once at the destination, the robot repositioned itself to precisely administer the liquid payload by amplifying the magnetic gradient, thus increasing chamber pressure and expelling its contents, which had a viscosity approximating 3 mPa·s. Additionally, we assessed the spread of the released liquid; even after commanding the robot to oscillate over the area more than 20 times, we detected negligible leakage (fig. S26).

In vitro performance test of capsule robot

We initiated our investigation by assessing the viability of our approach within a water tank. An ultrasonic probe was deployed to precisely locate and monitor the robot, and a combination of a manipulator and a magnet facilitated control over the spatial configuration of the external magnetic field. A tension linkage between the soft stripe and the piston exists, with the sensor's deformation mirroring the displacement of the piston. By modulating the distance between the magnet and the robot, we could alter the magnetic field strength, thereby inducing varying displacements of the piston. These variations in distance were detectable via the ultrasound probe, enabling us to accurately deduce changes in the chamber's volume. A thorough analysis of this process is detailed in the Supplementary Materials.

Fabrication of the viscometer bot

The viscometer bot was designed with three core components: a vibrating plate, a bottom plate, and an EUSS, all constructed from magnetic soft composite materials. The vibrating plate was fabricated by blending ferromagnetic NdFeB particles with Ecoflex 00-30 at an equal weight ratio of 1:1. This mixture was then poured into a 3D-printed mold to set. Once demolded and magnetized, the vibrating plate generated periodic oscillations under the influence of a rotational magnetic field. The bottom plate was crafted from a magnetic soft composite that combined PDMS in a 10:1 ratio of precursor to curing agent with unmagnetized NdFeB particles, ~5 μm in diameter, at a 1:3 weight ratio. The assembly process involved meticulously aligning all components within a custom 3D-printed support structure, ensuring optimal functionality and structural integrity.

Fabrication of the thermometer bot

The thermometer bot was composed of three primary components: a bottom plate, a bimetallic strip, and an EUSS. The bottom plate was crafted from a magnetic soft composite, blending PDMS in a 10:1 ratio of precursor to curing agent with ferromagnetic NdFeB particles, which are unmagnetized and average 5 μm in diameter, at a 1:3 weight ratio. The bimetallic strip features two distinct metals, each with differing thermal expansion coefficients: a copper-zinc alloy with a high expansion rate (18 to 20 $\times$ 10^{-6}/°C) and an iron-nickel alloy with a lower expansion rate (0.5 to 1.6 $\times$ 10^{-6}/°C). This strip is fashioned into a helix to enhance displacement at its end. Integration of these components, along with the sensor, was achieved using adhesive and supported by a 3D-printed framework. The sensor was meticulously attached to one side of the structure and on the other to the terminus of the helical bimetallic strip. A 3D mold aided in streamlining the assembly process, ensuring precision, and maintaining structural integrity.

Calibration of the thermometer bot

The calibration was performed using a water bath. Initially, the temperature of the hot plate was adjusted to 30°C. To monitor the surrounding temperature, one thermocouple probe was positioned close to the robots, and another was placed alongside the dish to ensure even heating throughout the water bath. Calibration began once the water bath temperature reached a stable 30°C, with a variance of less than 0.2°C between the two thermocouple readings. At this point, the ultrasound sensing system started capturing data from the robot. As the water bath's temperature gradually increased to 60°C, temperature readings from both the thermocouples and the robot were simultaneously monitored.

Ex vivo demonstration of the thermometer bot for inducing protein denaturation and porcine liver ablation

To assess the practicality of the thermometer bot, we conducted experiments that were designed to induce protein denaturation using egg whites as a model system. The thermometer bot was placed inside an eggshell filled with egg white and then submerged in a water tank. An rf coil was positioned beneath the tank, ~3 cm from the bottom. An ultrasound probe was used to visualize and detect frequency shifts in the EUSS, which indicated changes in the surrounding environment. In subsequent ex vivo tests involving porcine liver ablation, the robot was magnetically guided to the target site, which ensured that the ablation tip made direct contact with the liver tissue, as visualized under ultrasound imaging. The application of an rf signal heated the robot, causing temperature fluctuations during the ablation process. These fluctuations were continuously monitored via our ultrasound sensing system, which provided real-time feedback on the efficacy of the treatment.

In vivo demonstration of capsule robots

In this study, male New Zealand rabbits aged 8 to 10 weeks, weighing between 1.5 and 2.0 kg, were procured from Shenzhen Advanced Medical Services Co. Ltd. Before the commencement of the research, ethical approval was obtained from the institutional animal care and use committee (approval no. AAS C2304002 R). The capsule robots used in the study were sterilized with water and ethanol before deployment. All rabbits underwent an 8-hour fasting protocol and were administered a gastrointestinal antifoaming agent three times before the introduction of the capsule robots. During the experiment, the rabbits were kept hydrated and anesthetized to ensure their well-being. The movement of the capsule robots within the rabbits was controlled via a magnetic field, and their positions were continuously monitored using radiology imaging techniques (DSA, CGO-2100, Wandong). Upon reaching the targeted site, a customized ultrasound probe was used to image and monitor the release of the liquid sample.

In vivo demonstration of viscometer bots

Approval for the porcine experiments was obtained from the Committee on Animal Care at Shenzhen Lingfu Top Biotechnology Co. Ltd. (approval no. TOPGM-IACUC-2024-0070). The subjects, male Bama pigs weighing ~40 kg and aged 14 to 16 months, were placed on a clear liquid diet 24 hours before the experiments. On the day of the procedure, morning feeding was withheld, and an ultrasound defoamer was administered. Sedation was achieved using Telazol (tiletamine and zolazepam, 5 mg/kg), xylazine (2 mg/kg), and atropine (0.04 mg/kg). The experiment commenced with the deployment of the robot via endoscopy. To aid gastroscopy, to facilitate precise ultrasound imaging, and to ensure accurate positioning, PBS was injected through a gastric tube to expand the stomach. Once the robot was visualized via ultrasound imaging, a magnet was activated to generate a rotational magnetic field for calibration. The frequency signal from the EUSS was monitored for 10 s to confirm stability and consistency. To simulate changes in viscosity, fluids with a viscosity of 7 mPa·s were introduced via endoscopy, with continuous monitoring of frequency changes by our ultrasound system. At the end of the procedure, euthanasia was carried out using Fatal Plus (sodium pentobarbital) at a dosage of 115 to 120 mg/kg. Heart rate was monitored to confirm the efficacy of euthanasia.

In vivo demonstration of the thermometer bot

The preexperiment using large-animal models adhered to the methodology described previously. Access to the jejunum was facilitated via a midline laparotomy, with devices subsequently inserted into the stomach lumen through a small incision. Once the robot was visualized via ultrasound imaging, we commenced frequency collection from the EUSS. A thermometer was used as a reference for calibration. After securing a stable signal for more than 30 s, an rf signal was applied to wirelessly transfer heat, and the ultrasound probe continuously monitored the signal during the entire process. After the experiments, the animal was euthanized.

Statistical analysis

Experimental values were obtained from independent repeats (n) and were summarized as means ± SD in Microsoft Excel (v16.0), unless stated otherwise. Error bars represented the SD across n independent replicates (Fig. 5D). Linear regressions were performed in OriginPro (v10.0) or MATLAB (R2022b), where shown, and goodness-of-fit metrics [coefficient of determination (R^2) and RMSE] are reported in the relevant captions (figs. S28 and S31). For experiments with a single measurement ($n = 1$), only the raw value was reported.

Supplementary Materials

The PDF file includes:

Methods
Figs. S1 to S44
Tables S1 to S4
Legends for movies S1 to S10
References (*54*–*57*)

Other Supplementary Material for this manuscript includes the following:

Movies S1 to S10

REFERENCES AND NOTES

1. W. Hu, G. Z. Lum, M. Mastrangeli, M. Sitti, Small-scale soft-bodied robot with multimodal locomotion. *Nature* **554**, 81–85 (2018).
2. Y. Kim, H. Yuk, R. Zhao, S. A. Chester, X. Zhao, Printing ferromagnetic domains for untethered fast-transforming soft materials. *Nature* **558**, 274–279 (2018).
3. B. J. Nelson, S. Gervasoni, P. W. Chiu, L. Zhang, A. Zemmar, Magnetically actuated medical robots: An in vivo perspective. *Proc. IEEE* **110**, 1028–1037 (2022).
4. B. J. Nelson, I. K. Kaliakatsos, J. J. Abbott, Microrobots for minimally invasive medicine. *Annu. Rev. Biomed. Eng.* **12**, 55–85 (2010).
5. C. F. Guimarães, L. Gasperini, A. P. Marques, R. L. Reis, The stiffness of living tissues and its implications for tissue engineering. *Nat. Rev. Mater.* **5**, 351–370 (2020).
6. E. Maniou, S. Todros, A. Urciuolo, D. A. Moulding, M. Magnussen, I. Ampartzidis, L. Brandolino, P. Bellet, M. Giomo, P. G. Pavan, G. L. Galea, N. Elvassore, Quantifying mechanical forces during vertebrate morphogenesis. *Nat. Mater.* **23**, 1575–1581 (2024).
7. G. Zabow, S. Dodd, A. Koretsky, Shape-changing magnetic assemblies as high-sensitivity NMR-readable nanoprobes. *Nature* **520**, 73–77 (2015).
8. A. Mullard, Parsing clinical success rates. *Nat. Rev. Drug Discov.* **15**, 447–448 (2016).
9. X. Liu, L. Wang, Y. Xiang, F. Liao, N. Li, J. Li, J. Wang, Q. Wu, C. Zhou, Y. Yang, Y. Kou, Y. Yang, H. Tang, N. Zhou, C. Wan, Z. Yin, G. Z. Yang, G. Tao, J. Zang, Magnetic soft microfiberbots for robotic embolization. *Sci. Robot.* **9**, eadh2479 (2024).
10. N. Li, P. Fei, C. Tous, M. Rezaei Adariani, M.-L. Hautot, I. Ouedraogo, A. Hadjadj, I. P. Dimov, Q. Zhang, S. Lessard, Z. Nosrati, C. N. Ng, K. Saatchi, U. O. Häfeli, C. Tremblay, S. Kadoury, A. Tang, S. Martel, G. Soulez, Human-scale navigation of magnetic microrobots in hepatic arteries. *Sci. Robot.* **9**, eadh8702 (2024).
11. Q. Wang, Q. Wang, Z. Ning, K. F. Chan, J. Jiang, Y. Wang, L. Su, S. Jiang, B. Wang, B. Y. M. Ip, H. Ko, T. W. H. Leung, P. W. Y. Chiu, S. C. H. Yu, L. Zhang, Tracking and navigation of a microswarm under laser speckle contrast imaging for targeted delivery. *Sci. Robot.* **9**, eadh1978 (2024).
12. C. Hong, Z. Ren, C. Wang, M. Li, Y. Wu, D. Tang, W. Hu, M. Sitti, Magnetically actuated gearbox for the wireless control of millimeter-scale robots. *Sci. Robot.* **7**, eabo4401 (2022).
13. B. J. Nelson, B. R. Bendok, E. L. Turcotte, H. H. Batjer, Remote magnetic navigation enables precision telesurgery. *Sci. Robot.* **9**, eado3187 (2024).
14. V. Nair, A. N. Dalrymple, Z. Yu, G. Balakrishnan, C. J. Bettinger, D. J. Weber, K. Yang, J. T. Robinson, Miniature battery-free bioelectronics. *Science* **382**, eabn4732 (2023).
15. A. Abdigazy, M. Arfan, G. Lazzi, C. Sideris, A. Abramson, Y. Khan, End-to-end design of ingestible electronics. *Nat. Electron.* **7**, 102–118 (2024).
16. T.-Y. Huang, H. Gu, B. J. Nelson, Increasingly intelligent micromachines. *Annu. Rev. Control Robot. Auton. Syst.* **5**, 279–310 (2022).
17. K. Kwon, J. U. Kim, S. M. Won, J. Zhao, R. Avila, H. Wang, K. S. Chun, H. Jang, K. H. Lee, J.-H. Kim, S. Yoo, Y. J. Kang, J. Kim, J. Lim, Y. Park, W. Lu, T. I. Kim, A. Banks, Y. Huang, J. A. Rogers, A battery-less wireless implant for the continuous monitoring of vascular pressure, flow rate and temperature. *Nat. Biomed. Eng.* **7**, 1215–1228 (2023).
18. Z. Xie, F. Yuan, J. Liu, L. Tian, B. Chen, Z. Fu, S. Mao, T. Jin, Y. Wang, X. He, G. Wang, Y. Mo, X. Ding, Y. Zhang, C. Laschi, L. Wen, Octopus-inspired sensorized soft arm for environmental interaction. *Sci. Robot.* **8**, eadh7852 (2023).
19. Z. Zhakypov, K. Mori, K. Hosoda, J. Paik, Designing minimal and scalable insect-inspired multi-locomotion millirobots. *Nature* **571**, 381–386 (2019).
20. H. Cui, D. Yao, R. Hensleigh, H. Lu, A. Calderon, Z. Xu, S. Davaria, Z. Wang, P. Mercier, P. Tarazaga, X. R. Zheng, Design and printing of proprioceptive three-dimensional architected robotic metamaterials. *Science* **376**, 1287–1293 (2022).
21. Y. Kim, Y. Yang, X. Zhang, Z. Li, A. Vázquez-Guardado, I. Park, J. Wang, A. I. Efimov, Z. Dou, Y. Wang, J. Park, H. Luan, X. Ni, Y. S. Kim, J. Baek, J. J. Park, Z. Xie, H. Zhao, M. Gazzola, J. A. Rogers, R. Bashir, Remote control of muscle-driven miniature robots with battery-free wireless optoelectronics. *Sci. Robot.* **8**, eadd1053 (2023).
22. B. Gleich, I. Schmale, T. Nielsen, J. Rahmer, Miniature magneto-mechanical resonators for wireless tracking and sensing. *Science* **380**, 966–971 (2023).
23. H. Tang, Y. Yang, Z. Liu, W. Li, Y. Zhang, Y. Huang, T. Kang, Y. Yu, N. Li, Y. Tian, X. Liu, Y. Cheng, Z. Yin, X. Jiang, X. Chen, J. Zang, Injectable ultrasonic sensor for wireless monitoring of intracranial signals. *Nature* **630**, 84–90 (2024).
24. J. Liu, N. Liu, Y. Xu, M. Wu, H. Zhang, Y. Wang, Y. Yan, A. Hill, R. Song, Z. Xu, M. Park, Y. Wu, J. L. Ciatti, J. Gu, H. Luan, Y. Zhang, T. Yang, H. Y. Ahn, S. Li, W. Z. Ray, C. K. Franz, M. R. MacEwan, Y. Huang, C. W. Hammill, H. Wang, J. A. Rogers, Bioresorbable shape-adaptive structures for ultrasonic monitoring of deep-tissue homeostasis. *Science* **383**, 1096–1103 (2024).
25. C. Shi, V. Andino-Pavlovsky, S. A. Lee, T. Costa, J. Elloian, E. E. Konofagou, K. L. Shepard, Application of a sub–0.1-mm^3 implantable mote for in vivo real-time wireless temperature sensing. *Sci. Adv.* **7**, eabf6312 (2021).
26. T. Ö. Onur, "Ultrasound and ultrasonic imaging in medicine: Recent advances" in *Acoustic Technologies in Biology and Medicine*, A. Ozcelik, R. Becker, T. J. Huang, Eds. (Wiley, 2023), pp. 99–126; https://doi.org/10.1002/9783527841325.ch4.
27. J. Shim, P. Wang, K. Bertoldi, Harnessing instability-induced pattern transformation to design tunable phononic crystals. *Int. J. Solids Struct.* **58**, 52–61 (2015).
28. J. Liu, H. Guo, T. Wang, A review of acoustic metamaterials and phononic crystals. *Crystals* **10**, 305 (2020).
29. B. Tang, G. Hanna, P. Joice, A. Cuschieri, Identification and categorization of technical errors by Observational Clinical Human Reliability Assessment (OCHRA) during laparoscopic cholecystectomy. *Arch. Surg.* **139**, 1215–1220 (2004).
30. A. F. Khan, M. K. MacDonald, C. Streutker, C. Rowsell, J. Drake, T. Grantcharov, Tissue stress from laparoscopic grasper use and bowel injury in humans: Establishing intraoperative force boundaries. *BMJ Surg. Interv. Health Technol.* **3**, e000084 (2021).
31. M. Li, Y. Tang, R. H. Soon, B. Dong, W. Hu, M. Sitti, Miniature coiled artificial muscle for wireless soft medical devices. *Sci. Adv.* **8**, eabm5616 (2022).
32. D. Son, M. C. Ugurlu, M. Sitti, Permanent magnet array–driven navigation of wireless millirobots inside soft tissues. *Sci. Adv.* **7**, eabi8932 (2021).
33. M. A. Howard, S. M. Grady, R. C. Ritter, G. T. Gillies, E. G. Quate, J. A. Molloy, Magnetic movement of a brain thermoceptor. *Neurosurgery* **24**, 444–448 (1989).
34. R. Beatty, K. L. Mendez, L. H. Schreiber, R. Tarpey, W. Whyte, Y. Fan, S. T. Robinson, J. O'Dwyer, A. J. Simpkin, J. Tannian, P. Dockery, E. B. Dolan, E. T. Roche, G. P. Duffy, Soft robot–mediated autonomous adaptation to fibrotic capsule formation for improved drug delivery. *Sci. Robot.* **8**, eabq4821 (2023).
35. H. Joo, Y. Lee, J. Kim, J.-S. Yoo, S. Yoo, S. Kim, A. K. Arya, S. Kim, S. H. Choi, N. Lu, Soft implantable drug delivery device integrated wirelessly with wearable devices to treat fatal seizures. *Sci. Adv.* **7**, eabd4639 (2021).
36. K. Mendez, W. Whyte, B. R. Freedman, Y. Fan, C. E. Varela, M. Singh, J. C. Cintron-Cruz, S. E. Rothenbücher, J. Li, D. J. Mooney, E. T. Roche, Mechanoresponsive drug release from a flexible, tissue-adherent, hybrid hydrogel actuator. *Adv. Mater.* **36**, 2303301 (2023).
37. J. Koo, S. B. Kim, Y. S. Choi, Z. Xie, A. J. Bandodkar, J. Khalifeh, Y. Yan, H. Kim, M. K. Pezhouh, K. Doty, G. Lee, Y.-Y. Chen, S. M. Lee, D. D'Andrea, K. Jung, K. H. Lee, K. Li, S. Jo, H. Wang, J.-H. Kim, J. Kim, S.-G. Choi, W. J. Jang, Y. S. Oh, I. Park, S. S. Kwak, J.-H. Park, D. Hong, X. Feng, C.-H. Lee, A. Banks, C. Leal, H. M. Lee, Y. Huang, C. K. Franz, W. Z. Ray, M. M. Ewan, S.-K. Kang, J. A. Rogers, Wirelessly controlled, bioresorbable drug delivery device with active valves that exploit electrochemically triggered crevice corrosion. *Sci. Adv.* **6**, eabb1093 (2020).
38. S. S. Srinivasan, A. Alshareef, A. V. Hwang, Z. Kang, J. Kuosmanen, K. Ishida, J. Jenkins, S. Liu, W. A. M. Madani, J. Lennerz, A. Hayward, J. Morimoto, N. Fitzgerald, R. Langer, G. Traverso, RoboCap: Robotic mucus-clearing capsule for enhanced drug delivery in the gastrointestinal tract. *Sci. Robot.* **7**, eabp9066 (2022).
39. Y. Sun, W. Zhang, J. Gu, L. Xia, Y. Cao, X. Zhu, H. Wen, S. Ouyang, R. Liu, J. Li, Z. Jiang, D. Cheng, Y. Lv, X. Han, W. Qiu, K. Cai, E. Song, Q. Cao, L. Li, Magnetically driven capsules with multimodal response and multifunctionality for biomedical applications. *Nat. Commun.* **15**, 1839 (2024).
40. J. Sung, D. Luo, J. Wu, J. Ching, F. Chan, J. Lau, S. Mack, R. Ducharme, P. Okolo, M. Canto, A. Kalloo, S. Giday, Early clinical experience of the safety and effectiveness of Hemospray in achieving hemostasis in patients with acute peptic ulcer bleeding. *Endoscopy* **43**, 291–295 (2011).
41. C. K. Wong, C. W. K. Lam, A. K. L. Wu, W. K. Ip, N. L. S. Lee, I. H. S. Chan, L. C. W. Lit, D. S. C. Hui, M. H. M. Chan, S. S. C. Chung, J. J. Y. Sung, Plasma inflammatory cytokines

and chemokines in severe acute respiratory syndrome. *Clin. Exp. Immunol.* **136**, 95–103 (2004).
42. J. J. Y. Sung, E. J. Kuipers, H. B. El-Serag, Systematic review: The global incidence and prevalence of peptic ulcer disease. *Aliment. Pharmacol. Ther.* **29**, 938–946 (2009).
43. J. Min, Y. Yang, Z. Wu, W. Gao, Robotics in the gut. *Adv. Ther.* **3**, 1900125 (2020).
44. H. Yabuno, K. Higashino, M. Kuroda, Y. Yamamoto, Self-excited vibrational viscometer for high-viscosity sensing. *J. Appl. Phys.* **116**, 124305 (2014).
45. R. Pringle, "Gastric mucus viscosity and peptic ulcer," in *Mucus in Health and Disease*, M. Elstein, D. V. Parke, Eds. (Springer, 1977), pp. 227–237; https://link.springer.com/chapter/10.1007/978-1-4613-4172-7_17.
46. R. H. Soon, Z. Yin, M. A. Dogan, N. O. Dogan, M. E. Tiryaki, A. C. Karacakol, A. Aydin, P. Esmaeili-Dokht, M. Sitti, Pangolin-inspired untethered magnetic robot for on-demand biomedical heating applications. *Nat. Commun.* **14**, 3320 (2023).
47. C.-C. Yeh, Y.-J. Yang, "An RF-powered wireless micro-heater integrated with acrylate-composite-based temperature regulatory for hyperthermia treatment" in *2020 IEEE 33rd International Conference on Micro Electro Mechanical Systems* (*MEMS*) (IEEE, 2020), pp. 357–360; https://ieeexplore.ieee.org/document/9056427.
48. S. R. Madhvapathy, M. I. Bury, L. W. Wang, J. L. Ciatti, R. Avila, Y. Huang, A. K. Sharma, J. A. Rogers, Miniaturized implantable temperature sensors for the long-term monitoring of chronic intestinal inflammation. *Nat. Biomed. Eng.* **8**, 1040–1052 (2024).
49. S. R. Madhvapathy, J.-J. Wang, H. Wang, M. Patel, A. Chang, X. Zheng, Y. Huang, Z. J. Zhang, L. Gallon, J. A. Rogers, Implantable bioelectronic systems for early detection of kidney transplant rejection. *Science* **381**, 1105–1112 (2023).
50. C. Brace, Thermal tumor ablation in clinical use. *IEEE Pulse* **2**, 28–38 (2011).
51. E. M. Knavel, C. L. Brace, Tumor ablation: Common modalities and general practices. *Tech. Vasc. Interv. Radiol.* **16**, 192–200 (2013).
52. H. Rhim, G. D. Dodd III, K. N. Chintapalli, B. J. Wood, D. E. Dupuy, J. L. Hvizda, P. E. Sewell, S. N. Goldberg, Radiofrequency thermal ablation of abdominal tumors: Lessons learned from complications. *Radiographics* **24**, 41–52 (2004).
53. H. Nakagawa, W. S. Yamanashi, J. V. Pitha, M. Arruda, X. Wang, K. Ohtomo, K. J. Beckman, J. H. McClelland, R. Lazzara, W. M. Jackman, Comparison of in vivo tissue temperature profile and lesion geometry for radiofrequency ablation with a saline-irrigated electrode versus temperature control in a canine thigh muscle preparation. *Circulation* **91**, 2264–2273 (1995).
54. X. Liu, N. Chen, J. Jiao, J. Liu, Pneumatic soft phononic crystals with tunable band gap. *Int. J. Mech. Sci.* **240**, 107906 (2023).
55. X. Liu, G. J. Pettway, L. K. McCauley, P. X. Ma, Pulsatile release of parathyroid hormone from an implantable delivery system. *Biomaterials* **28**, 4124–4131 (2007).
56. V. Iacovacci, I. Tamadon, E. F. Kauffmann, S. Pane, V. Simoni, L. Marziale, M. Aragona, L. Cobuccio, M. Chiarugi, P. Dario, S. del Prato, L. Ricotti, F. Vistoli, A. Menciassi, A fully implantable device for intraperitoneal drug delivery refilled by ingestible capsules. *Sci. Robot.* **6**, eabh3328 (2021).
57. D. Zaharia, Structural analysis of helical bimetallic strip thermostat. *Int. J. Mod. Manuf. Technol.* **3**, 99–106 (2011).

Acknowledgments

Funding: This work was supported by the National Natural Science Foundation of China (52188102, T2350001, 52173280, and 524B2073), the Young Elite Scientists Sponsorship Program by China Association of Science and Technology (2024QNRC001), Huazhong University of Science and Technology Interdisciplinary Research Support Program (2023JCYJ044), the Taihu Lake Innovation Fund for Future Technology, HUST (2023A3), and the Research Impact Fund (project no. R4015-21). L.Z. thanks the Hong Kong Research Grants Council (RGC), Research Fellow Scheme (project no. RFS2122-4S03), and the Strategic Topics Grant (project no. STG1/E-401/23-N) for the support. We also thank the Multi-scale Medical Robotics Centre (MRC), InnoHK at the Hong Kong Science Park, and the SIAT-CUHK Joint Laboratory of Robotics and Intelligent Systems for support. **Author contributions:** X.L., H.T., J.Z., and L.Z. conceived the idea and designed the research. X.L. and H.T. constructed the experimental platform. X.L., H.T., L.H., and N.L. constructed the viscosity sensing and temperature sensing. X.L. and H.T. performed other experiments and analyzed the data. X.L., H.T., J.Z., and L.Z. wrote the manuscript. All authors participated in drafting the manuscript and discussing and interpreting the data. **Competing interests:** J.Z., X.L., and H.T. have a provisional patent application on the fundamental principles and designs of the EUSS for wireless miniature machines (CN patent, application no. 2025111027862 and 2025111028371). The other authors declare that they have no competing financial interests. **Data and materials availability:** All data needed to support the conclusions of this manuscript are included in the main text or Supplementary Materials or on Zenodo at https://doi.org/10.5281/zenodo.16757742.

Submitted 12 November 2024
Accepted 19 August 2025
Published 17 September 2025
10.1126/scirobotics.adu4851

Science Robotics

Miniature magneto-ultrasonic machines for wireless robotic sensing and manipulation

Xurui Liu, Hanchuan Tang, Na Li, Linjie He, Ye Tian, Bo Hao, Junnan Xue, Chaoyu Yang, Joseph Jao Yiu Sung, Li Zhang, and Jianfeng Zang

Sci. Robot. **10** (106), eadu4851. DOI: 10.1126/scirobotics.adu4851

Science Robotics (ISSN 2470-9476) is published by the American Association for the Advancement of Science. 1200 New York Avenue NW, Washington, DC 20005. The title *Science Robotics* is a registered trademark of AAAS.